ResearchGate

See discussions, stats, and author profiles for this publication at: https://www.researchgate.net/publication/353700640

# Impact of mid-gap states on transport in single-crystal Graphene-MoS2 heterojunctions integrated into a multi-FET architecture

**Preprint** · August 2021

CITATIONS
0

READS
127

**11 authors**, including:

Gaia Ciampalini
Università di Pisa
**4** PUBLICATIONS **18** CITATIONS

SEE PROFILE

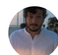
Guido Menichetti
Università di Pisa
**31** PUBLICATIONS **204** CITATIONS

SEE PROFILE

Vaidotas Mišeikis
Istituto Italiano di Tecnologia
**107** PUBLICATIONS **2,280** CITATIONS

SEE PROFILE

Alessandro Pitanti
Italian National Research Council
**128** PUBLICATIONS **1,683** CITATIONS

SEE PROFILE

All content following this page was uploaded by Gaia Ciampalini on 10 January 2022.

The user has requested enhancement of the downloaded file.

arXiv:2108.02116v1 [cond-mat.mes-hall] 4 Aug 2021

# Impact of mid-gap states on transport in single-crystal Graphene-$MoS_2$ heterojunctions integrated into a multi-FET architecture

Gaia Ciampalini,[*,†,‡,¶] Filippo Fabbri,[¶] Guido Menichetti,[‡,†] Luca Buoni,[†] Simona Pace,[‡,§] Vaidotas Mišeikis,[‡,§] Alessandro Pitanti,[¶] Dario Pisignano,[†,¶] Camilla Coletti,[‡,§] Alessandro Tredicucci,[†,¶] and Stefano Roddaro[†,¶]

†*Dipartimento di Fisica "E. Fermi," Università di Pisa, Largo B. Pontecorvo 3, I-56127 Pisa, Italy*

‡*Graphene Labs, Istituto Italiano di Tecnologia, Via Morego 30, I-16163 Genova, Italy*

¶*NEST, CNR—Istituto Nanoscienze and Scuola Normale Superiore, piazza San Silvestro 12, I-56127 Pisa, Italy*

§*Center for Nanotechnology Innovation @NEST, Istituto Italiano di Tecnologia, Piazza San Silvestro 12, I-56127 Pisa, Italy*

E-mail: gaia.ciampalini@phd.unipi.it

## Abstract

We demonstrate a graphene-$MoS_2$ architecture integrating multiple field-effect transistors and we independently probe and correlate the conducting properties of van der Waals coupled graphene-$MoS_2$ contacts with the ones of the $MoS_2$ channels. Devices are fabricated starting from high-quality single-crystal monolayers grown by chemical vapor deposition and characterized by scanning Raman and photoluminescence spectroscopies. Transconductance curves of $MoS_2$ are compared with the current-voltage characteristics of graphene contact stripes, revealing a significant suppression of transport on the $n$-side of the transconductance curve. Based on ab-initio modeling, the effect is understood in terms of trapping by sulfur vacancies, which counter-intuitively depends on the field-effect, even though the graphene contact layer is positioned between the backgate and the $MoS_2$ channel.

## Keywords

graphene, $MoS_2$, heterostructure, field-effect, single-crystal

## Letter

Van der Waals (vdW) heterostructures, formed when two or more atomically-thin crystals are bonded by vdW interaction,[1] are intriguing architectures, enabled by the discovery of two-dimensional (2D) materials, such as graphene, hexagonal boron nitride, and transition metal dichalcogenides (TMDs). Within this family, peculiar junctions can be obtained when graphene is used as a contact material for a TMD monolayer. While the interface between a TMD and a conventional, bulk metallic electrode tends to display Schottky behavior due to intrinsic and extrinsic Fermi pinning phenomena,[2–4] vdW graphene-TMD junctions yield well-behaved linear transport characteristics.[5] This contacting approach has been successful in improving TMD-based devices.[6] Nev-

ertheless, the exact physics behind graphene-TMD vdW junctions is still debated[7–9] and difficult to probe in a direct way. In particular, devices typically include only two contacts, which makes effects on the transport characteristics due to the interface not easy to distinguish from those due to the resistivity of the two-dimensional materials, since typically only the global conductance of the device can be measured.

Charge transfer phenomena,[10] strain,[11] and charge trapping in defects,[12–14] might also play an important role. Furthermore, in the case of field-effect devices, the low density of states in the vicinity of the Dirac point leads to weak screening properties despite the metallic nature of graphene.[15] This implies that a non-trivial response to field effect can be observed, and exploited in novel device concepts.[16,17] Gating on graphene-$MoS_2$ heterostructures has been widely investigated from a numerical[18] and experimental[5,19–21] point of view, and in different stacking configurations. Indeed, the reciprocal electrostatic screening of the junction materials can remarkably affect the contact resistance, and it was shown theoretically that $MoS_2$ can screen the field effect on graphene, or not, depending on the order of the specific stacking sequence.[18] Nevertheless, to the best of our knowledge, direct experimental evidence of how the formation of vdW interfaces leads to changes in the trasport properties of the individual materials involved in field-effect transistor (FET) devices is still missing.

The progress of large-scale chemical vapor deposition (CVD) techniques gives the opportunity to investigate vdW interfaces from a different angle. High-quality and large-scale monocrystalline flakes of graphene[22,23] and TMDs[24,25] can be reproducibly grown. When this technique is associated with a patterning of the seed points, predictable flake arrays of chosen sizes can be achieved,[26] opening to a promising pathway to the fabrication of multiple parallel devices combining different 2D materials. In this Letter, we take advantage of this opportunity to demonstrate a novel graphene-dichalcogenide architecture where a monocrystalline $MoS_2$ channel is contacted by a large

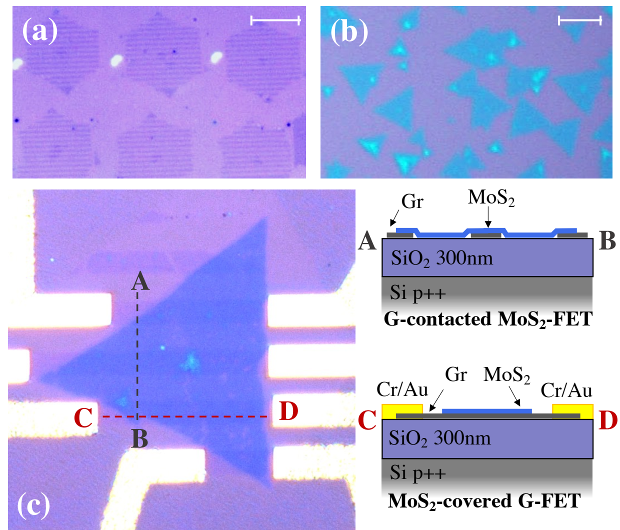


Figure 1: **Multi-FET device architecture.** (a) Monocrystalline contact stripes obtained by patterning a periodic array of graphene CVD flakes (scale bar is 100 $\mu$m). (b) Monocrystalline CVD $MoS_2$ flakes before transfer onto the $SiO_2$/Si substrate (scale bar is 50 $\mu$m). (c) Optical picture of one of the studied devices implementing a multiple FET structure, as visible in the cross-section sketches: graphene multi-contact $MoS_2$ FET (AB section) and $MoS_2$-covered graphene FET (CD section).

number of monocrystalline graphene stripes, each of them crossing the whole $MoS_2$ channel as schematized in Fig. 1. Each stripe can thus act as ohmic contact for a $MoS_2$ backgated FET (see cross-section AB in Fig. 1), and be simultaneously contacted at its terminations to implement an additional $MoS_2$-covered graphene FET (cross-section CD in Fig. 1). This structure can so act as a $MoS_2$ FET and as a set of graphene FETs at the same time, which will be referred to as a *multi-FET* in the following. Such unique arrangement allows a first independent study of the conducting properties to be performed for the different components of graphene-$MoS_2$ systems, highlighting a suppression of the electron-side transconductance in $MoS_2$-covered graphene, in coincidence with the conducting threshold of free $MoS_2$ in the main device channel. This behavior is apparently at odd with recent predictions for defect-free $MoS_2$,[18] nonetheless it can be understood in terms of a gate-driven trapping by sulfur va-

cancies which further highlights the non-trivial weak screening properties of graphene.

The multi-FET fabrication starts from a square array of $\approx 150\,\mu$m-wide single-crystal monolayer graphene flakes, with a spacing of $200\,\mu$m. Arrays are grown on Cu foil via CVD[26] and then transferred on a p++ Si substrate covered by 300 nm thermal $SiO_2$ following the procedure described in Ref. 22. Each flake is patterned into a set of $5\,\mu$m-wide and $5\,\mu$m-spaced stripes via electron-beam lithography followed by reactive ion-etching, leading to the structures visible in Fig. 1a. Single-crystal $MoS_2$ monolayer flakes with an average size of $\approx 50\,\mu$m were grown via CVD following Ref. 27 and 28 (see Fig. 1b). Given the chosen spacing between the stripes, the process typically yields various devices with $4-5$ contacts and, since the flakes are triangular, with an uneven coverage of the graphene stripes. The transfer process employed for $MoS_2$ is very similar to the one for graphene except for the delamination step, which was obtained by immersing the sample in a 1 M solution of NaOH rather than by an electrochemical method.[27] After the transfer, excess $MoS_2$ flakes were removed by a further dry etching step and, finally, metallic Cr/Au (10/50 nm) electrodes were defined by electron-beam lithography and thermal evaporation. Each fabrication process yields various devices in parallel, one of them visible in Fig. 1c. Further details about fabrication are reported in the experimental methods in the Supporting Information (Fig. S1a shows a schematic of the fabrication procedure).

Both the patterning procedures and the formation of vdW interfaces can significantly perturb the properties of the 2D materials. For this reason, photoluminescence (PL) and Raman spectroscopy were employed to characterize the 2D crystals at relevant device processing steps. In Fig. 2a-c, we report Raman spectra of a typical transferred $MoS_2$ flake and analyze the influence of the graphene contact stripes. The characteristic $A_{1G}$ and $E_{2G}$ modes visible in panel (a) exhibit a strong dependence on thickness[31] and their separation $\Delta\omega \simeq 19$ cm$^{-1}$ is in good agreement with the expected monolayer nature of the $MoS_2$ flake. Raman data contain also information on the local doping and strain, which can be analyzed based on the correlation plot in Fig. 2b, where the position of the $A_{1G}$ peak is plotted against the one of $E_{2G}$.[29] Mean Raman shifts of the $E_{2G}$ and $A_{1G}$ peaks in graphene-free regions are $384.5 \pm 0.3$ cm$^{-1}$ and $403.3 \pm 0.4$ cm$^{-1}$, respectively. These values are quite close to the neutrality point, located at the intersection between zero strain and zero doping line ($E_{2G} = 384.6 \pm 0.2\,\mathrm{cm}^{-1}$ and $A_{1G} = 402.7 \pm 0.2\,\mathrm{cm}^{-1}$).[29] Interestingly, Raman shifts from regions where $MoS_2$ overlaps graphene ($E_{2G} = 383.4 \pm 0.5\,\mathrm{cm}^{-1}$ and $A_{1G} = 404.3 \pm 0.3\,\mathrm{cm}^{-1}$) indicate a variation in tensile strain distribution of $\approx 0.10-0.35\%$ and a sizable electron reduction of $(3.0 \pm 1.8) \times 10^{12}$ cm$^{-2}$. Thanks to the sensitivity of the $A_{1G}$ peak on doping,[32] the spatial doping modulation of $MoS_2$ due to graphene can be directly appreciated in the map of the $A_{1G}$ position in Fig. 2c. The map is shown in overlay to an optical picture of the flake, to highlight the good correlation between the map patterns and the position of the graphene stripes. Consistent evidences are obtained from graphene Raman data shown in Fig. 2d-f. In panel (d), graphene spectra in the presence/absence of $MoS_2$ are compared. Both curves show a single sharp Lorentzian-shaped $2D$ peak, which is a typical signature of monolayer graphene,[33] and no $D$ peak, which indicates a negligible density of defects.[34] The absence of defects was confirmed for all the fabrication steps (see Supporting Information Fig. S2). We also note that when graphene is covered in $MoS_2$ (orange curve), a strong baseline appears below the Raman peaks due to the $MoS_2$ PL signal. As in the case of $MoS_2$, strain and doping profiles can be derived from the Raman data,[30] based on the correlation plot of the $2D$ and $G$ modes reported in Fig. 2e, see Supporting Information for additional correlation plots (Fig. S1c-f). The positions of the $G$ and $2D$ peaks in regions free from $MoS_2$ are $1582.7 \pm 0.9\,\mathrm{cm}^{-1}$ and $2676.2 \pm 2.2\,\mathrm{cm}^{-1}$, respectively, corresponding to a $p$-type doping. Differently, Raman data collected in $MoS_2$-covered regions ($1585.4 \pm 1.5\,\mathrm{cm}^{-1}$ and $2685.8 \pm 3.7\,\mathrm{cm}^{-1}$ for the $G$ and $2D$ peaks, respectively) fall on the strain line, thus indicating a neutralization

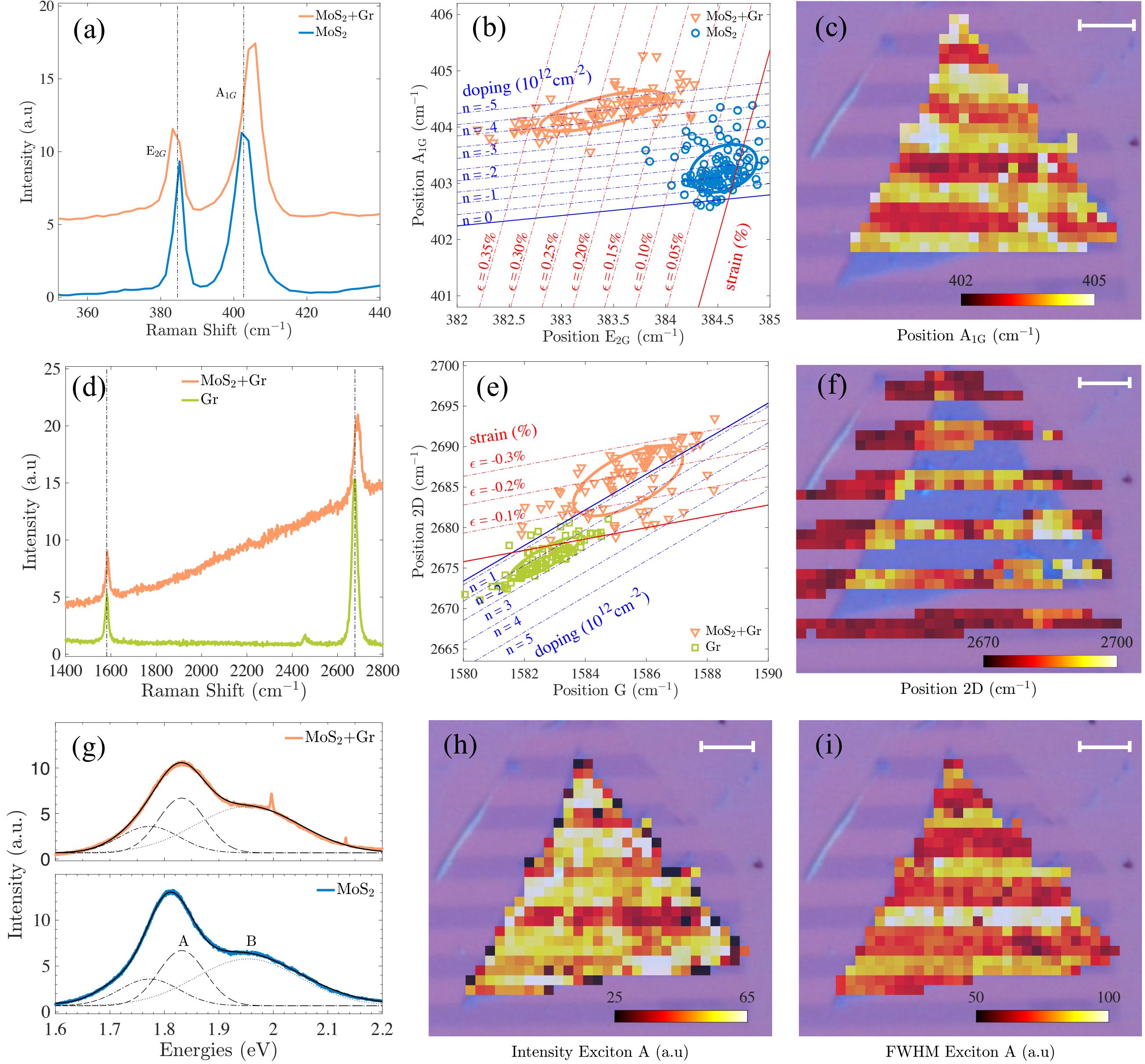

Figure 2: **Optical characterization of the $MoS_2$-graphene structures.** (a) $MoS_2$ Raman spectra after transfer on top of the graphene stripes: both spectra from $MoS_2$ on top of graphene (orange) and graphene-free $MoS_2$ (blue) are reported. (b) Correlation plot of the position of $A_{1G}$ as a function of the position of $E_{2G}$. Zero strain and zero doping line are taken from Ref. 29 (514.5 nm laser excitation).(c) Map of the position of $A_{1G}$. (d) Raman spectra of graphene after the $MoS_2$ transfer: both spectra in the presence (orange) and absence (green) of the $MoS_2$ overlayer are reported. (e) Correlation plot of the position of $2D$ peak as a function of the position of $G$ peak. Zero strain and zero doping line are taken from Ref. 30 (514.5 nm laser excitation) (f) Map of the position of $2D$ peak. (g) PL spectra of $MoS_2$ both in a region where it overlaps graphene (orange) and in a graphene-free region (blue). Gaussian fits of $A$ and $B$ excitons are shown in dashed and dot-dashed lines respectively. (h) Map of the position-dependent quenching of the $A$ exciton signal. (i) Map of the position-dependent $A$ exciton broadening. All maps are shown in overlay to an optical image of the analyzed flake, scalebars in the panels correspond to $10\,\mu$m.

of graphene. The variation of mean peaks positions corresponds to an electron increase of $(2.3 \pm 1.5) \times 10^{12}$ cm$^{-2}$ and to a variation of strain nature from compressive to tensile. The spatial modulation of the doping can be seen from the $2D$ peak position map in panel (f), showing a good correlation with the position of the $MoS_2$ flake. A modified strain is also observed, turning from slightly tensile to compressive $\approx 0.10 - 0.30\%$. We note that the doping and strain trends observed where $MoS_2$ and graphene overlap are opposite and thus consistent. We further highlight that while Raman data clearly indicate an electron transfer from $MoS_2$ to graphene, absolute equilibrium carrier densities are not obvious to be determined, due to the presence of photo-excited carriers during the Raman measurements. The formation of the heterojunction can be further investigated based on the PL spectra of $MoS_2$, which are reported in Fig. 2g. Three main peaks are highlighted by Gaussian deconvolution. These peaks are attributed to the A exciton (1.81 eV), the B exciton (1.94 eV) and the trion (1.71 eV).[35,36] We observe that the presence of graphene modifies the $MoS_2$ response and the signal of the $A$ exciton is quenched when $MoS_2$ is coupled to graphene (orange curve) with respect to stand-alone $MoS_2$ (blue curve): indeed, a lowering of the $A$ intensity by $\approx$ 30% and a lineshape broadening from $\approx 66$ meV to $\approx 96$ meV is retrieved. The spatial modulation of the effect can be directly appreciated from the maps of the intensity and width of the $A$ exciton in Fig. 2h and Fig. 2i, respectively. Additional spectroscopic data are reported in the Supporting Information (S5-S9).

The graphene stripes form ohmic contacts to the $MoS_2$ channel and lead, at room temperature and in vacuum conditions ($P < 10^{-5}$ mbar), to highly linear two-wire IV curves over the $\pm 2$ V range. In Fig. 3a, we report the $I_{SD}$ vs $V_{SD}$ characteristics of a representative $MoS_2$ FETs, measured as a function of the gate voltage ($V_G$) in the $0 - 80$ V range. The transfer characteristic in Fig. 3b indicates a positive threshold voltage, with a sizable clockwise hysteresis, as frequently reported in literature for FETs based on 2D materials and

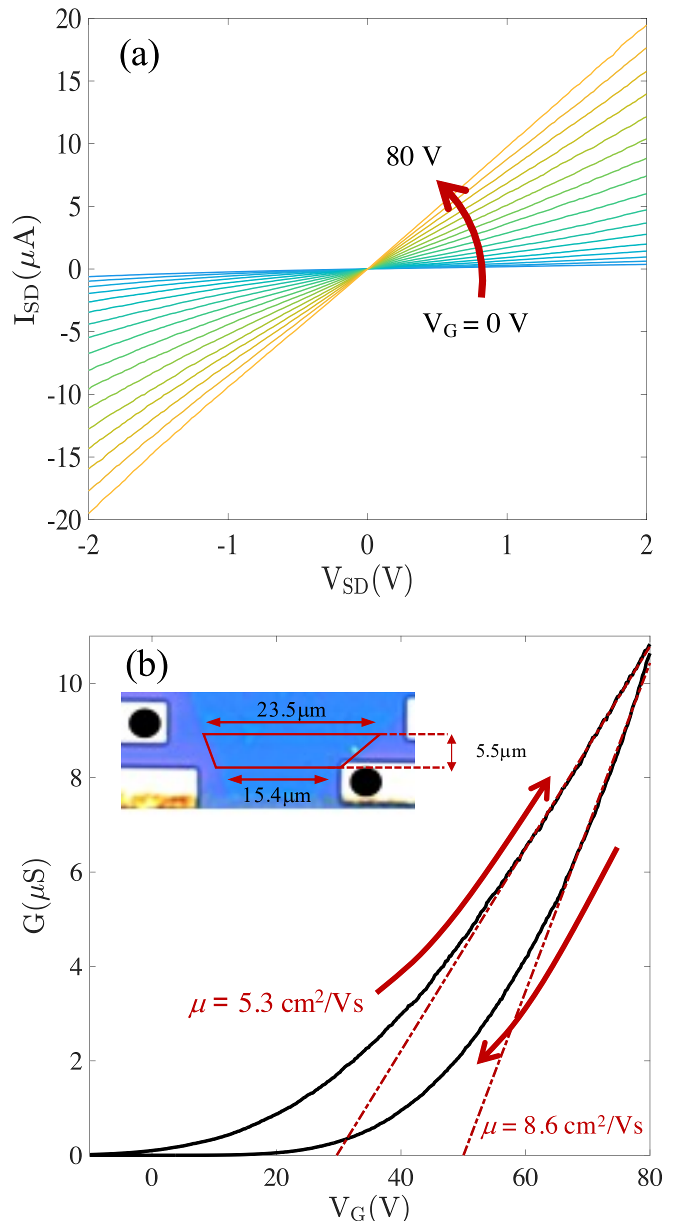


Figure 3: **Transport characteristics of $MoS_2$**. (a) Room-temperature IV characteristics of the $MoS_2$ channel as function of the gate voltage $V_G$ in the $0 - 80$ V range. (b) Transfer characteristics showing a strong hysteresis, with red arrows indicating the sweep direction. Red dashed lines are the linear fits used to estimate the field-effect mobility for each of the two curves. Inset: an optical image of the measured device, with a sketch of the channel geometry and contacts highlighted by black dots.

nanowires,[37–41] as well as in Kelvin probe microscopy experiments.[42] The effect is generally ascribed to the slow dynamics of trap states leading to a time-dependent screening

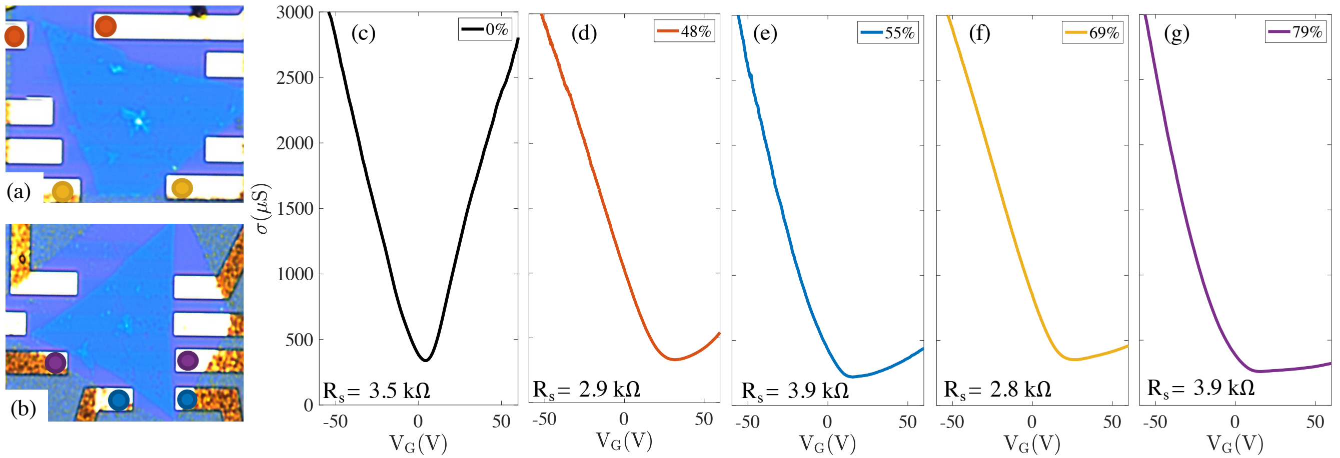


Figure 4: **Effect of the $MoS_2$ overlayer on electron transport in the graphene contact stripes**. (a-b) Optical images of the two devices used to estimate the effect of different $MoS_2$ coverage levels on conduction in the graphene stripes. Used contacts are highlighted by colored dots. (c-g) Transfer characteristics of the graphene stripes for different $MoS_2$ coverages ranging from 0% to 79%. The curve colors match the ones used to highlight the contacts in panels (a) and (b): red 48%, blue 55%, yellow 69%, purple 79%; the black curve corresponds to a reference $MoS_2$-free graphene stripe (device image not shown).

of the field effect of the gate. Trap states may have several origins, including defects at the $SiO_2$ substrate interface,[41] adsorbates,[40] or $MoS_2$ point defects.[39] In our devices, possible sources of traps include interfaces between $MoS_2$, graphene and $SiO_2$ (see AFM data in the Supporting Information S-10) as also S vacancies in $MoS_2$, which are know to occur in quite large densities (typically few $10^{13}\,\text{cm}^{-2}$) in CVD flakes.[43,44] The field-effect mobility of $MoS_2$ carrier can be estimated from the transfer characteristic according to

$$\mu = \frac{dG}{dV_G}\frac{L^2}{C_G}, \tag{1}$$

where $C_G$ is the capacitance and the $MoS_2$ trapezoid channel sketched in the inset of Fig. 3b is approximated as a rectangle with a length $L = 5.5 \pm 0.3\,\mu$m and width $W = 19.5 \pm 0.5\,\mu$m. Considering both curves in the hysteresis loop, we extract two mobility values $\approx 5.3\,\text{cm}^2/\text{Vs}$ and $\approx 8.6\,\text{cm}^2/\text{Vs}$. Similar analysis on different FETs yielded field-effect mobilities in the range $5.3 - 6.6\,\text{cm}^2/\text{Vs}$. Given that gate hysteresis generally indicates that part of the gate-induced carriers end in charge traps, field-effect measurements are known to overestimate the carrier density induced in the channel and to underestimate mobility.[38,45] Both the mobility values above should thus be considered as a lower bound to the true room temperature electron mobility in the specific $MoS_2$ flake. The method also neglects the effect of contact resistances, which may lead to a mobility underestimation but are not expected to have a significant effect in the explored transport regime, based on preliminary four-wire measurement data.

Our multi-FET devices were specifically designed for comparing the $MoS_2$ transport characteristics with the electron configuration in the graphene stripes, which play here the dual role of the contact in the $MoS_2$ FET and of the channel in $MoS_2$-covered graphene FETs. The IVs of all our graphene stripes are found to be highly linear (data not shown) and in Fig. 4 we report the transfer characteristic of various graphene FETs as a function of the $V_G$, from which we obtain a mobility $\approx 4085\,\text{cm}^2/\text{Vs}$. In the plot sequence (c-g), we compare the conductivity of stripes characterized by a different $MoS_2$ coverage: conductivity is calculated from the total resistance using the geometrical form factor of the stripe and contact resistances are estimated by comparing the $p$-side of the gate sweeps; $MoS_2$ coverage is quantified

from the ratio between the area of the $MoS_2$-graphene and the graphene regions, see optical pictures in Fig. 4a-b. Coverage goes from 0% ($MoS_2$-free graphene in panel (c)) to 79% (panel (g)). A clear trend is observed in the transfer characteristics: curves go from a conventional ambipolar behavior in panel (c) to a limit of strongly quenched $n$-type conduction for the largest coverage in panel (g). The observation of a quenching of field effect in graphene-TMD heterostructures has been reported in the literature, for instance in $WS_2$-graphene heterostructures and in graphene functionalized with different materials, such as $TiO_2$ or organic molecules as well.[13,14,46–48] On the other hand, the observed behavior is somewhat puzzling since, ideally, $MoS_2$ should not affect carrier density in graphene when positioned on top of back-gated graphene due to the reciprocal screening in the vdW heterostructure.[18]

Our analysis allows for identifying the origin of this apparent discrepancy as due to vacancies in TMDs,[43,44] which are also likely a main cause of the hysteretic behavior reported in Fig. 3. Using Density Functional Theory (DFT),[53] we made an ab-initio analysis of the electronic states of graphene-$MoS_2$[54] in the presence of sulfur vacancies: these have an energy that falls in the gap[55] of $MoS_2$ and are located at a distance of few Angstroms from graphene, so their effect is hard to evaluate without a first-principles approach (see Methods and Supporting Information for further details). Numerical calculations were performed using a density of S-vacancies of $\rho_v \approx 7.5 \times 10^{13}\,\mathrm{cm}^{-2}$. In Fig. 5a we report the electronic band structure and projected density of states (DOS) of the graphene-$MoS_2$ heterostructure for $V_G = 0$: as visibile in the plot, the Fermi energy of the system lays in the proximity of $MoS_2$ mid-gap states generated by the S-vacancies. This suggests that such states may influence the mobile carrier density induced in the graphene layer by the gate when $V_G \neq 0$. This is confirmed by calculations performed at different values of $V_G$, where the distribution of the resulting excess of carrier density is evaluated by means of the topological analysis of the electron density, using the Bader procedure.[49,50,56,57] As shown in Fig. 5b, even if $MoS_2$ is placed on top of graphene, it affects the carrier density induced by the gate in the graphene layer. In particular, the $n$-side of the field-effect response is reduced by $\approx 50\%$; this, combined with the likely increased scattering caused by the large DOS close to the Fermi energy, clearly reproduces the behavior reported in Fig. 4. In Fig. 5c-d, the atomistic structure and the model of the typical setup for a field-effect measurement are shown. The charge density isosurfaces, together with the planar averaged carrier charge density, give a pictorial view of the different behavior with negative and positive backgate voltages. We point out that our results do not contradict, but rather complement, the conclusion drawn in recent literature:[18] calculations also show that no charge transfer is obtained in the case of defect-free $MoS_2$ since in that limit the TMD cannot support any electron state in the relevant energy range (see Supporting Information Fig. S8). Nonetheless, it is interesting to highlight that, in the presence of vacancies, a TMD overlayer can indeed have a remarkable impact on the backgate response of these vdW heterostructures and of devices based on them, extending the range of non-trivial consequences of the weak screening properties of graphene.

In conclusion, we have demonstrated a graphene-$MoS_2$ architecture integrating multiple graphene-contacted $MoS_2$ FETs and $MoS_2$-covered graphene FETs and used it to correlate the field-effect characteristics of a $MoS_2$ monolayer with the conducting properties of graphene used to contact it. Such a study cannot be performed in a conventional FET structure since the individual resistive contributes cannot be discriminated in any obvious and direct way. Our results show that $MoS_2$ can affect the field-effect conduction of a back-gated graphene monolayer, even when placed on top of the vdW stack, and the suppression of conduction in the graphene stripes is observed over a gate voltage range which is consistent with the conduction threshold of the $MoS_2$ channel. This behavior is explained in terms of a filling of sulfur vacancies in the $MoS_2$, as supported by ab-initio calculations.

**Methods.** Further details on the fabrication

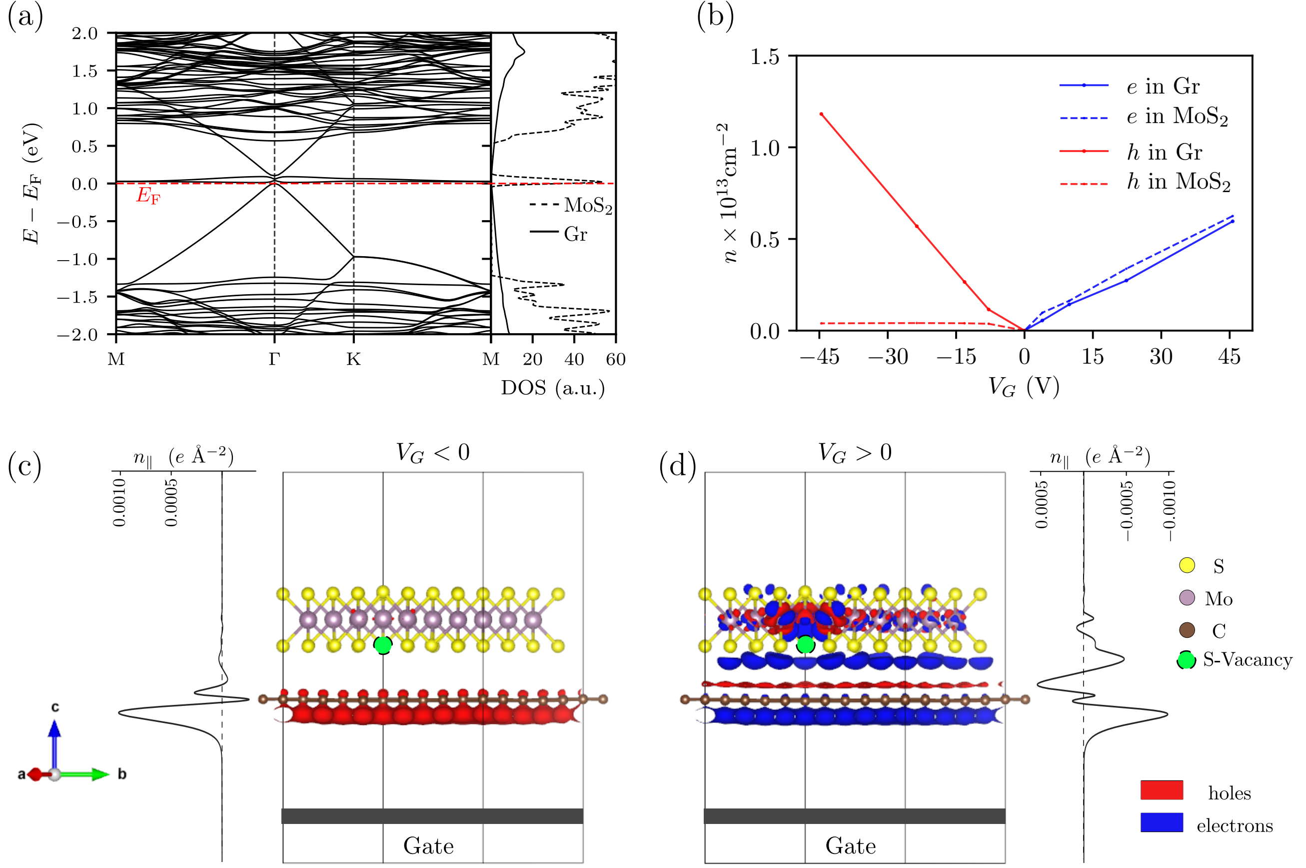


Figure 5: **Field-effect response in the presence of S-vacancies.** The impact of sulfur vacancies was simulated by removing one S atom from a $MoS_2$ supercell (density of S-vacancies of $\rho_v \approx 7.5 \times 10^{13}\,\mathrm{cm}^{-2}$). (a) Supercell band structure and projected density of states (DOS) of the Graphene-$MoS_2$ interface; the red dashed line indicates the Fermi energy $E_\mathrm{F}$. In the DOS plot, pristine graphene is indicated with a continuous line and the S-vacancy appears as a peak close to the Dirac point. (b) Field-effect induced charge distribution as a function of gate voltage $V_G$, evaluated as the difference between the gated ($V_G \neq 0$) and ungated case ($V_G = 0$); the topological analysis of the electron density was done by means of the Bader procedure.[49–52] The solid (dashed) red line indicates the excess holes on the graphene ($MoS_2$) monolayer, while the solid (dashed) blue line indicates the excess electrons. In order to mimic the experimental values, the values of $V_G$ are rescaled considering that there is a 300 $nm$ thick layer of $SiO_2$ between the metal gate and the Graphene-$Mo_2$ interface. (c-d) Side view of the gated Graphene-$MoS_2$ interface. In the two panels, the charge isosurface for $V_G < 0$ (left) and $V_G > 0$ (right) is evaluated as the difference between the charge densities for the gated and ungated limit; on the two sides, the averaged surface charge density is shown considering S-vacancies with doping $n \approx -1.2 \times 10^{13}$ $cm^{-2}$ which corresponts to $V_G \approx +45$ V in panel b . The location of the S-vacancy is marked by the green ball.

are reported in the Supporting Information (S3-S4). The properties of graphene and $MoS_2$ were monitored by Raman and photoluminescence spectroscopy, using a *Renishaw InVia* spectrometer equipped with a 532 nm laser. Laser power was $\approx 1\,\text{mW}$ and the typical acquisition time was $4\,\text{s}$.[58] Transport measurements were performed in a vacuum chamber using source-measure units K4200 and K2614B and a Femto DDPCA-300 current preamplifier. We investigated how field-effect doping affects the electronic structure carrying out DFT calculations by using the QUANTUM ESPRESSO (QE).[59–63] To obtain information on the charge transfer between the two moieties (Graphene-$MoS_2$) we performed a topological analysis of the electron density by means of the Bader procedure[49,50] as implemented in CRITIC2.[51,52] See Supporting Information for further details.[22,27,53,62–75]

**Acknowledgement** G.M. thanks G. Grosso for useful discussions. G.C. thanks L. Martini for useful discussions. SR and AT acknowledge the support of the Italian Ministry of Research through the PRIN projects "Quantum 2D" and "Monstre 2D", respectively. G.M. acknowledges the "IT center" of the University of Pisa, the HPC center (Franklin) of the IIT of Genova, and the allocation of computer resources from CINECA, through the "ISCRA C" projects "HP10C9JF51", "HP10CI1LTC", "HP10CY46PW", "HP10CMQ8ZK". The research leading to these results has received funding from the European Union's Horizon 2020 research and innovation program under grant agreement no. 881603-Graphene Core3.

# Supporting Information Available

Experimental and theoretical methods, additional Raman data, additional photoluminescence data, atomic force miscroscopy measurement, additional DFT results.

# References

(1) Geim, A. K.; Grigorieva, I. V. Van der Waals heterostructures. *Nature* **2013**, *499*, 419–425.

(2) Kim, C.; Moon, I.; Lee, D.; Choi, M. S.; Ahmed, F.; Nam, S.; Cho, Y.; Shin, H.-J.; Park, S.; Yoo, W. J. Fermi Level Pinning at Electrical Metal Contacts of Monolayer Molybdenum Dichalcogenides. *ACS Nano* **2017**, *11*, 1588–1596.

(3) Sotthewes, K.; van Bremen, R.; Dollekamp, E.; Boulogne, T.; Nowakowski, K.; Kas, D.; Zandvliet, H. J. W.; Bampoulis, P. Universal Fermi-Level Pinning in Transition-Metal Dichalcogenides. *The Journal of Physical Chemistry C* **2019**, *123*, 5411–5420.

(4) Das, S.; Chen, H.-Y.; Penumatcha, A. V.; Appenzeller, J. High Performance Multilayer $MoS_2$ Transistors with Scandium Contacts. *Nano Letters* **2013**, *13*, 100–105.

(5) Liu, Y.; Wu, H.; Cheng, H.-C.; Yang, S.; Zhu, E.; He, Q.; Ding, M.; Li, D.; Guo, J.; Weiss, N. O.; Huang, Y.; Duan, X. Toward Barrier Free Contact to Molybdenum Disulfide Using Graphene Electrodes. *Nano Letters* **2015**, *15*, 3030–3034.

(6) Chuang, H.-J.; Tan, X.; Ghimire, N. J.; Perera, M. M.; Chamlagain, B.; Cheng, M. M.-C.; Yan, J.; Mandrus, D.; Tománek, D.; Zhou, Z. High Mobility $WSe_2$ p- and n-Type Field-Effect Transistors Contacted by Highly Doped Graphene for Low-Resistance Contacts. *Nano Lett.* **2014**, *14*, 3594–3601.

(7) Yu, W. J.; Li, Z.; Zhou, H.; Chen, Y.; Wang, Y.; Huang, Y.; Duan, X. Vertically stacked multi-heterostructures of layered materials for logic transistors and complementary inverters. *Nat. Mater.* **2013**, *12*, 246–252.

(8) Kwak, J. Y.; Hwang, J.; Calderon, B.; Alsalman, H.; Munoz, N.; Schutter, B.;

Spencer, M. G. Electrical Characteristics of Multilayer $MoS_2$ FET's with $MoS_2$/Graphene Heterojunction Contacts. *Nano Lett.* **2014**, *14*, 4511–4516.

(9) Tian, H.; Tan, Z.; Wu, C.; Wang, X.; Mohammad, M. A.; Xie, D.; Yang, Y.; Wang, J.; Li, L.-J.; Xu, J.; Ren, T.-L. Novel Field-Effect Schottky Barrier Transistors Based on Graphene-$MoS_2$ Heterojunctions. *Sci. Rep.* **2014**, *4*, 5951.

(10) Dappe, Y. J.; Almadori, Y.; Dau, M. T.; Vergnaud, C.; Jamet, M.; Paillet, C.; Journot, T.; Hyot, B.; Pochet, P.; Grévin, B. Charge transfers and charged defects in $WSe_2$/graphene-SiC interfaces. *Nanotechnology* **2020**, *31*, 255709.

(11) Liu, X.; Li, Z. Electric Field and Strain Effect on Graphene-$MoS_2$ Hybrid Structure: Ab Initio Calculations. *J. Phys. Chem. Lett.* **2015**, *6*, 3269–3275.

(12) Han, Y.; Wu, Z.; Xu, S.; Chen, X.; Wang, L.; Wang, Y.; Xiong, W.; Han, T.; Ye, W.; Lin, J.; Cai, Y.; Ho, K. M.; He, Y.; Su, D.; Wang, N. Probing Defect-Induced Midgap States in $MoS_2$ Through Graphene–$MoS_2$ Heterostructures. *Adv. Mater. Interfaces* **2015**, *2*, 1500064.

(13) Piccinini, G.; Forti, S.; Martini, L.; Pezzini, S.; Miseikis, V.; Starke, U.; Fabbri, F.; Coletti, C. Deterministic direct growth of $WS_2$ on graphene arrays. *2D Materials* **2019**, *7*, 014002.

(14) Avsar, A.; Tan, J. Y.; Taychatanapat, T.; Balakrishnan, J.; Koon, G. K. W.; Yeo, Y.; Lahiri, J.; Carvalho, A.; Rodin, A. S.; O'Farrell, E. C. T.; Eda, G.; Castro Neto, A. H.; Özyilmaz, B. Spin–orbit proximity effect in graphene. *Nature Communications* **2014**, *5*, 4875.

(15) Li, L. H.; Tian, T.; Cai, Q.; Shih, C.-J.; Santos, E. J. G. Asymmetric electric field screening in van der Waals heterostructures. *Nat. Commun.* **2018**, *9*, 1271.

(16) Zhu, X.; Li, D.; Liang, X.; Lu, W. D. Ionic modulation and ionic coupling effects in $MoS_2$ devices for neuromorphic computing. *Nat. Mater.* **2019**, *18*, 141–148.

(17) Krishnaprasad, A.; Choudhary, N.; Das, S.; Dev, D.; Kalita, H.; Chung, H.-S.; Aina, O.; Jung, Y.; Roy, T. Electronic synapses with near-linear weight update using $MoS_2$/graphene memristors. *Applied Physics Letters* **2019**, *115*, 103104.

(18) Stradi, D.; Papior, N. R.; Hansen, O.; Brandbyge, M. Field Effect in Graphene-Based van der Waals Heterostructures: Stacking Sequence Matters. *Nano Letters* **2017**, *17*, 2660–2666.

(19) Cui, X. et al. Multi-terminal transport measurements of $MoS_2$ using a van der Waals heterostructure device platform. *Nat. Nanotechnol.* **2015**, *10*, 534–540.

(20) Lee, G.-H.; Cui, X.; Kim, Y. D.; Arefe, G.; Zhang, X.; Lee, C.-H.; Ye, F.; Watanabe, K.; Taniguchi, T.; Kim, P.; Hone, J. Highly Stable, Dual-Gated $MoS_2$ Transistors Encapsulated by Hexagonal Boron Nitride with Gate-Controllable Contact, Resistance, and Threshold Voltage. *ACS Nano* **2015**, *9*, 7019–7026.

(21) Bertolazzi, S.; Krasnozhon, D.; Kis, A. Nonvolatile Memory Cells Based on $MoS_2$/Graphene Heterostructures. *ACS Nano* **2013**, *7*, 3246–3252.

(22) Giambra, M. A.; Mišeikis, V.; Pezzini, S.; Marconi, S.; Montanaro, A.; Fabbri, F.; Sorianello, V.; Ferrari, A. C.; Coletti, C.; Romagnoli, M. Wafer-Scale Integration of Graphene-Based Photonic Devices. *ACS Nano* **2021**, *15*, 3171–3187.

(23) Wang, M.; Luo, D.; Wang, B.; Ruoff, R. S. Synthesis of Large-Area Single-Crystal Graphene. *Trends Chem.* **2021**, *3*, 15–33.

(24) Schram, T. et al. $WS_2$ transistors on 300 mm wafers with BEOL compatibility. 2017 47th European Solid-State Device

Research Conference (ESSDERC). 2017; pp 212–215.

(25) Cun, H.; Macha, M.; Kim, H.; Liu, K.; Zhao, Y.; LaGrange, T.; Kis, A.; Radenovic, A. Wafer-scale MOCVD growth of monolayer $MoS_2$ on sapphire and $SiO_2$. *Nano Res.* **2019**, *12*, 2646–2652.

(26) Miseikis, V.; Bianco, F.; David, J.; Gemmi, M.; Pellegrini, V.; Romagnoli, M.; Coletti, C. Deterministic patterned growth of high-mobility large-crystal graphene: a path towards wafer scale integration. *2D Mater.* **2017**, *4*, 021004.

(27) Conti, S. et al. Low-voltage 2D materials-based printed field-effect transistors for integrated digital and analog electronics on paper. *Nature Communications* **2020**, *11*, 3566.

(28) Kim, H.; Han, G. H.; Yun, S. J.; Zhao, J.; Keum, D. H.; Jeong, H. Y.; Ly, T. H.; Jin, Y.; Park, J.-H.; Moon, B. H.; Kim, S.-W.; Lee, Y. H. Role of alkali metal promoter in enhancing lateral growth of monolayer transition metal dichalcogenides. **2017**, *28*, 36LT01.

(29) Michail, A.; Delikoukos, N.; Parthenios, J.; Galiotis, C.; Papagelis, K. Optical detection of strain and doping inhomogeneities in single layer $MoS_2$. *Applied Physics Letters* **2016**, *108*, 173102.

(30) Lee, J. E.; Ahn, G.; Shim, J.; Lee, Y. S.; Ryu, S. Optical separation of mechanical strain from charge doping in graphene. *Nature Communications* **2012**, *3*, 1024.

(31) Lee, C.; Yan, H.; Brus, L. E.; Heinz, T. F.; Hone, J.; Ryu, S. Anomalous Lattice Vibrations of Single- and Few-Layer $MoS_2$. *ACS Nano* **2010**, *4*, 2695–2700.

(32) Chakraborty, B.; Bera, A.; Muthu, D. V. S.; Bhowmick, S.; Waghmare, U. V.; Sood, A. K. Symmetry-dependent phonon renormalization in monolayer $MoS_2$ transistor. *Phys. Rev. B* **2012**, *85*, 161403.

(33) Ferrari, A. C.; Meyer, J. C.; Scardaci, V.; Casiraghi, C.; Lazzeri, M.; Mauri, F.; Piscanec, S.; Jiang, D.; Novoselov, K. S.; Roth, S.; Geim, A. K. Raman Spectrum of Graphene and Graphene Layers. *Phys. Rev. Lett.* **2006**, *97*, 187401.

(34) Cançado, L. G.; Jorio, A.; Ferreira, E. H. M.; Stavale, F.; Achete, C. A.; Capaz, R. B.; Moutinho, M. V. O.; Lombardo, A.; Kulmala, T. S.; Ferrari, A. C. Quantifying Defects in Graphene via Raman Spectroscopy at Different Excitation Energies. *Nano Letters* **2011**, *11*, 3190–3196.

(35) Mouri, S.; Miyauchi, Y.; Matsuda, K. Tunable Photoluminescence of Monolayer $MoS_2$ via Chemical Doping. *Nano Letters* **2013**, *13*, 5944–5948.

(36) Splendiani, A.; Sun, L.; Zhang, Y.; Li, T.; Kim, J.; Chim, C.-Y.; Galli, G.; Wang, F. Emerging Photoluminescence in Monolayer $MoS_2$. *Nano Letters* **2010**, *10*, 1271–1275.

(37) Mitta, S. B.; Choi, M. S.; Nipane, A.; Ali, F.; Kim, C.; Teherani, J. T.; Hone, J.; Yoo, W. J. Electrical characterization of 2D materials-based field-effect transistors. **2020**, *8*, 012002.

(38) Roddaro, S.; Ercolani, D.; Safeen, M. A.; Suomalainen, S.; Rossella, F.; Giazotto, F.; Sorba, L.; Beltram, F. Giant Thermovoltage in Single InAs Nanowire Field-Effect Transistors. *Nano Letters* **2013**, *13*, 3638–3642.

(39) Bartolomeo, A. D.; Genovese, L.; Giubileo, F.; Iemmo, L.; Luongo, G.; Foller, T.; Schleberger, M. Hysteresis in the transfer characteristics of $MoS_2$ transistors. *2D Materials* **2017**, *5*, 015014.

(40) Late, D. J.; Liu, B.; Matte, H. S. S. R.; Dravid, V. P.; Rao, C. N. R. Hysteresis in Single-Layer $MoS_2$ Field Effect Transistors. *ACS Nano* **2012**, *6*, 5635–5641.

(41) Vu, Q. A.; Fan, S.; Lee, S. H.; Joo, M.-K.; Yu, W. J.; Lee, Y. H. Near-zero hysteresis and near-ideal subthreshold swing in h-BN encapsulated single-layer $MoS_2$ field-effect transistors. *2D Mater.* **2018**, *5*, 031001.

(42) Wang, Y.; Li, D.; Lai, X.; Liu, B.; Chen, Y.; Wang, F.; Wang, R.; Zhang, L. Direct observation of the hysteretic Fermi level modulation in monolayer $MoS_2$ field effect transistors. *Current Applied Physics* **2020**, *20*, 298–303.

(43) Hong, J. et al. Exploring atomic defects in molybdenum disulphide monolayers. *Nat. Commun.* **2015**, *6*, 6293.

(44) Qiu, H.; Xu, T.; Wang, Z.; Ren, W.; Nan, H.; Ni, Z.; Chen, Q.; Yuan, S.; Miao, F.; Song, F.; Long, G.; Shi, Y.; Sun, L.; Wang, J.; Wang, X. Hopping transport through defect-induced localized states in molybdenum disulphide. *Nat. Commun.* **2013**, *4*, 2642.

(45) Pitanti, A.; Roddaro, S.; Vitiello, M. S.; Tredicucci, A. Contacts shielding in nanowire field effect transistors. *Journal of Applied Physics* **2012**, *111*, 064301.

(46) Yan, Z.; Yao, J.; Sun, Z.; Zhu, Y.; Tour, J. M. Controlled Ambipolar-to-Unipolar Conversion in Graphene Field-Effect Transistors Through Surface Coating with Poly(ethylene imine)/Poly(ethylene glycol) Films. *Small* **2012**, *8*, 59–62.

(47) Li, H.; Zhang, Q.; Liu, C.; Xu, S.; Gao, P. Ambipolar to Unipolar Conversion in Graphene Field-Effect Transistors. *ACS Nano* **2011**, *5*, 3198–3203.

(48) Kim, M.; Safron, N. S.; Huang, C.; Arnold, M. S.; Gopalan, P. Light-Driven Reversible Modulation of Doping in Graphene. *Nano Letters* **2012**, *12*, 182–187.

(49) *Atoms in Molecules: A Quantum Theory*; Oxford University Press, Oxford, 1990.

(50) Gatti, C. Chemical bonding in crystals: new directions. *Z. Kristallogr. Cryst. Mater.* **2005**, *220*, 399–457.

(51) Otero-de-la Roza, A.; Johnson, E. R.; Luaña, V. Critic2: A program for real-space analysis of quantum chemical interactions in solids. *Comput. Phys. Commun.* **2014**, *185*, 1007–1018.

(52) Otero-de-la Roza, A.; Blanco, M. A.; Pendás, A. M.; Luaña, V. Critic: a new program for the topological analysis of solid-state electron densities. *Comput. Phys. Commun.* **2009**, *180*, 157–166.

(53) *Solid State Physics*; Academic Press, London, 2014.

(54) Giuliani, G.; Vignale, G. *Quantum Theory of the Electron Liquid*; Cambridge University Press: Cambridge, 2005.

(55) Bussolotti, F.; Yang, J.; Kawai, H.; Wong, C. P. Y.; Goh, K. E. J. Impact of S-Vacancies on the Charge Injection Barrier at the Electrical Contact with the $MoS_2$ Monolayer. *ACS Nano* **2021**, *15*, 2686–2697.

(56) Menichetti, G.; Colle, R.; Gatti, C.; Grosso, G. Heterointerface Electronic States and Charge Transport of Crystalline N,N'-1H,1H'-Perfluorobutil Dicyanoperylene Diimide in Field-Effect Transistor Configuration. *J. Phys. Chem. C* **2016**, *120*, 12083–12091.

(57) Menichetti, G.; Colle, R.; Grosso, G. Strain Modulation of Band Offsets at the PCBM/P3HT Heterointerface. *J. Phys. Chem. C* **2017**, *121*, 13707–13716.

(58) Pace, S.; Ferrera, M.; Convertino, D.; Piccinini, G.; Magnozzi, M.; Mishra, N.; Forti, S.; Bisio, F.; Canepa, M.; Fabbri, F.; Coletti, C. Thermal stability of monolayer $WS_2$ in BEOL conditions. **2021**, *4*, 024002.

(59) Giannozzi, P. et al. QUANTUM ESPRESSO: a modular and open-source

software project for quantum simulations of materials. *J. Phys.: Condens. Matter* **2009**, *21*, 395502.

(60) Giannozzi, P. et al. Advanced capabilities for materials modelling with Quantum ESPRESSO. *J. Phys.: Condens. Matter* **2017**, *29*, 465901.

(61) Giannozzi, P.; Baseggio, O.; Bonfà, P.; Brunato, D.; Car, R.; Carnimeo, I.; Cavazzoni, C.; de Gironcoli, S.; Delugas, P.; Ferrari Ruffino, F.; Ferretti, A.; Marzari, N.; Timrov, I.; Urru, A.; Baroni, S. Quantum ESPRESSO toward the exascale. *J. Chem. Phys.* **2020**, *152*, 154105.

(62) Brumme, T.; Calandra, M.; Mauri, F. Electrochemical doping of few-layer ZrNCl from first principles: Electronic and structural properties in field-effect configuration. *Phys. Rev. B* **2014**, *89*, 245406.

(63) Brumme, T.; Calandra, M.; Mauri, F. First-principles theory of field-effect doping in transition-metal dichalcogenides: Structural properties, electronic structure, Hall coefficient, and electrical conductivity. *Phys. Rev. B* **2015**, *91*, 155436.

(64) Prandini, G.; Marrazzo, A.; Castelli, I. E.; Mounet, N.; Marzari, N. Precision and efficiency in solid-state pseudopotential calculations. *Npj Comput. Mater.* **2018**, *4*, 72.

(65) Lejaeghere, K. et al. Reproducibility in density functional theory calculations of solids. *Science* **2016**, *351*, aad3000.

(66) Schlipf, M.; Gygi, F. Optimization algorithm for the generation of ONCV pseudopotentials. *Comput. Phys. Commun.* **2015**, *196*, 36–44.

(67) Dal Corso, A. Pseudopotentials periodic table: From H to Pu. *Comput. Mater. Sci.* **2014**, *95*, 337–350.

(68) Garrity, K. F.; Bennett, J. W.; Rabe, K. M.; Vanderbilt, D. Pseudopotentials for high-throughput DFT calculations. *Comput. Mater. Sci.* **2014**, *81*, 446–452.

(69) Perdew, J. P.; Burke, K.; Ernzerhof, M. Generalized Gradient Approximation Made Simple. *Phys. Rev. Lett.* **1996**, *77*, 3865–3868.

(70) Grimme, S. Semiempirical GGA-type density functional constructed with a long-range dispersion correction. *J. Comput. Chem.* **2006**, *27*, 1787–1799.

(71) Marzari, N.; Vanderbilt, D.; De Vita, A.; Payne, M. C. Thermal Contraction and Disordering of the Al(110) Surface. *Phys. Rev. Lett.* **1999**, *82*, 3296–3299.

(72) Monkhorst, H. J.; Pack, J. D. Special points for Brillouin-zone integrations. *Phys. Rev. B* **1976**, *13*, 5188–5192.

(73) Colle, R.; Menichetti, G.; Grosso, G. Graphene on clean (0001) -quartz: Numerical determination of a minimum energy path from metal to semiconductor. *physica status solidi (b)* **2016**, *253*, 1799–1807.

(74) Wakabayashi, N.; Smith, H. G.; Nicklow, R. M. Lattice dynamics of hexagonal $MoS_2$ studied by neutron scattering. *Phys. Rev. B* **1975**, *12*, 659–663.

(75) Momma, K.; Izumi, F. *VESTA3* for three-dimensional visualization of crystal, volumetric and morphology data. *J. Appl. Crystallogr.* **2011**, *44*, 1272–1276.

# Graphical TOC Entry

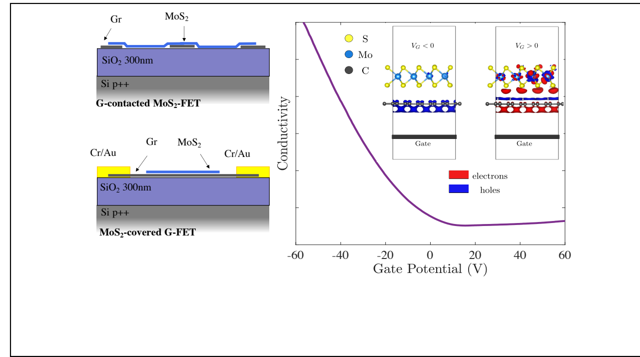




View publication stats